ACS APPLIED MATERIALS & INTERFACES

www.acsami.org

Research Article

Revolutionizing Airborne Virus Defense: Electromagnetic MXene-Coated Air Filtration for Superior Aerosol Viral Removal

Fangzhou Liu, Qingquan Ma, Md Mohidul Alam Sabuj, Shih-Hsiang Yen, Dheeban Govindan, Jianan Gao, Mengqiang Zhao,* Menachem Elimelech, and Wen Zhang*

Cite This: *ACS Appl. Mater. Interfaces* 2024, 16, 10148−10157

Read Online

ACCESS | Metrics & More | Article Recommendations | Supporting Information

ABSTRACT: The COVID-19 pandemic sparked public health concerns about the transmission of airborne viruses. Current methods mainly capture pathogens without inactivation, leading to potential secondary pollution. Herein, we evaluated the inactivation performance of a model viral species (MS2) in simulated bioaerosol by an electromagnetically enhanced air filtration system under a 300 kHz electromagnetic induction field. A nonwoven fabric filter was coated with a 2D catalyst, MXene ($Ti_3C_2T_x$), at a coating density of 4.56 mg·cm^{-2} to absorb electromagnetic irradiation and produce local heating and electromagnetic field for microbial inactivation. The results showed that the MXene-coated air filter significantly enhanced the viral removal efficiency by achieving a log removal of 3.4 ± 0.15 under an electromagnetic power density of 369 W·cm^{-2}. By contrast, the pristine filter without catalyst coating only garnered a log removal of 0.3 ± 0.04. Though the primary antimicrobial mechanism is the local heating as indicated by the elevated surface temperature of 72.2 ± 4 °C under the electromagnetic field, additional nonthermal effects (e.g., dielectrophoresis) on enhanced viral capture during electromagnetically enhanced filtration were investigated by COMSOL simulation to delineate the potential transmission trajectories of bioaerosol. The results provide unique insights into the mechanisms of pathogen control and thus promote alternative solutions for preventing the transmission of airborne pathogens.

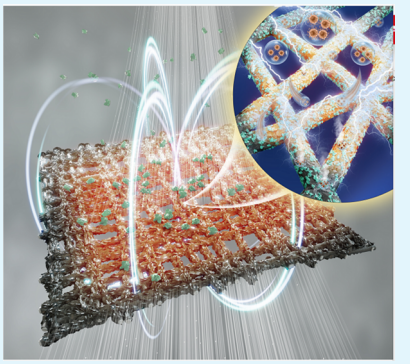

KEYWORDS: *MXene, airborne virus, electromagnetic, air filtration, inductive heating*

INTRODUCTION

The coronavirus outbreak in 2019 (COVID-19) has profoundly affected global health and raised concerns about the risks of airborne pathogens. Bioaerosols are the main vector that carries the viral agents during air transmission.[1,2] Residential settings present heightened risks to inhabitants due to indoor bioaerosol contamination, which is often introduced when infected individuals sneeze or cough. Thus, building heating, ventilation, and air-conditioning (HVAC) systems become increasingly important for intercepting the transmission of these airborne pathogens.

Typically, air purification by HVAC relies on adsorbent-based air filters (e.g., fiberglass filters, activated carbon filters, and polypropylene filters) to capture bioaerosols mainly due to adsorption and depth filtration.[3] Although traditional filters like high-MERV-rated filters and filtering facepiece respirators (FFRs) are frequently used in healthcare settings, they possess limited abilities to capture and neutralize small viruses that might slip through the filter.[4] Additionally, bioaerosols collected on the filter surface may not be inactivated and the captured pathogens could survive and spread, posing a secondary risk of reproliferation and human infection. Therefore, effective air sterilization and purification are essential for reducing the risks of airborne pathogen spread and safeguarding public health against potential respiratory diseases.

A method for inactivating pathogens in air filters involves the use of antiviral surface coatings. For instance, tannic acid-coated HEPA filters have been demonstrated to effectively capture influenza viral particles, achieving a remarkable in-solution virus capture efficiency of up to 2723 PFU·mm^{-2} in 10 min.[5] Metals such as copper and silver, recognized for their potent antimicrobial traits against a broad range of microorganisms, serve as alternative effective coatings.[6,7] However, over time, these filter coatings can diminish in potency and efficacy due to the accumulation of viral/bacterial residues or dust, which obstructs the direct interaction between the antimicrobial coating and the microorganisms.[8]

Alternatively, ultraviolet (UV) disinfection,[9] electrically driven disinfection,[10−12] and electromagnetic radiation disinfection,[13] are coupled with air filtration to enhance the antimicrobial activity. For instance, the combination of HEPA

Received: December 5, 2023
Revised: February 2, 2024
Accepted: February 2, 2024
Published: February 16, 2024

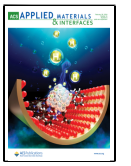

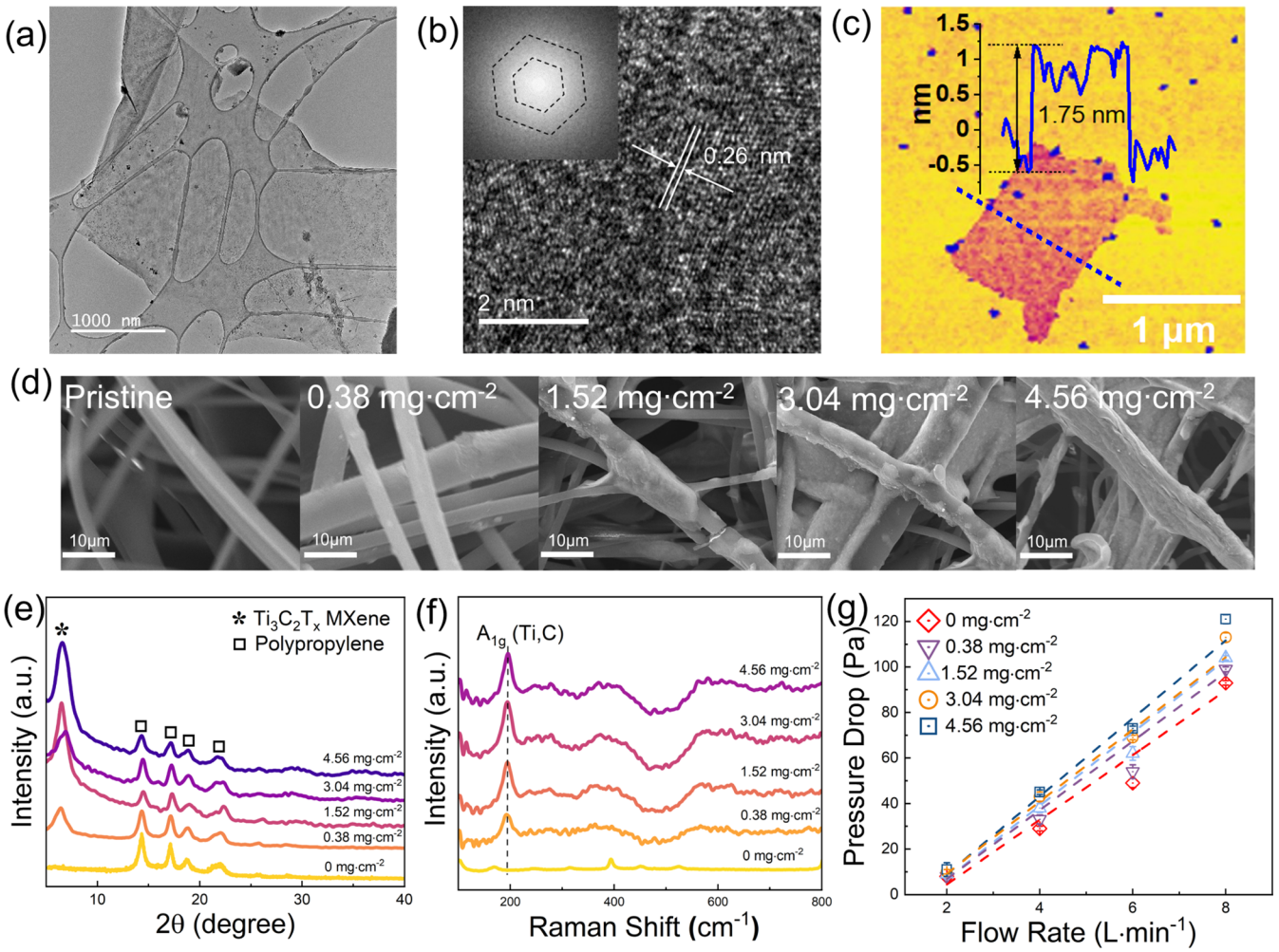

Figure 1. (a) HRTEM image of a single piece of MXene nanosheet. (b) Enlarged HRTEM image and the selected area electron diffraction (SAED) pattern of MXene nanosheet. (c) AFM image a single piece of MXene nanosheet. (d) SEM images of MXene-coated nonwoven polypropylene filters with different coating densities. (e) XRD spectra and (f) Raman spectra of MXene-coated air filters with the coating densities of 0.38, 1.52, 3.04, and 4.56 mg·cm^{-2}. (g) Pressure drops of MXene-coated filters with different MXene coating densities and flow rates.

filtration and UV−C light (254 nm) has achieved 93% removal of Severe Acute Respiratory Syndrome Coronavirus 2 (SARS-CoV-2) in bioaerosols.[9] However, the effectiveness of UV−C irradiation in eliminating microorganisms can diminish with rising relative humidity and air dust levels, as these factors might absorb or obstruct UV rays, offering protection to airborne pathogens.[14,15] Electrically driven disinfection, such as electrochemical oxidation,[10] electrostatic separation,[11] and triboelectric disinfection,[12] utilizes the production of potent oxidants (e.g., ozone, H_2O_2, and radicals), electroporation, and joule heating on electrode surface, which may suffer from electrode fouling and secondary pollution.

Compared with the above air purification, electromagnetic radiation can penetrate deeply into materials and selectively energize electromagnetic adsorption materials (e.g., carbonaceous materials,[16] transition metal oxides,[17] semiconductors,[18] and ferromagnetic metals[19]). Both thermal heating and nonthermal chemical oxidation effects could be imposed on the captured aerosols or microorganisms. Electromagnetic waves in the microwave range, with wavelengths ranging from 1 mm to 1 m, have been used in air filtration for airborne virus inactivation,[1] for example, by applying 375 W microwave irradiation to an HVAC filter mounted on a silicon carbide (SiC) disk.[13] Though microwave disinfection for air purification is still in its infancy, it has demonstrated great potential for broad microbial disinfection and high economic viability.[20] However, due to the high frequency (2.45 GHz) and relatively short wavelength, application of commercial microwave disinfection requires a cavity to prevent microwave leakage and human exposure.

Low-frequency alternating electromagnetic waves with longer wavelength (>1 m) are becoming attractive. Particularly, electromagnetic induction heating has been harnessed for diverse applications, including biomedical technologies for controlled drug release,[21] disease treatment by magnetic hyperthermia,[22] membrane distillation,[23] and catalytic reactions.[19,24] Induction heating of materials occurs through three mechanisms: hysteresis heating during magnetization reversal, magnetic field heating in superparamagnetic nanoparticles, and eddy currents induced by an alternating magnetic field in conductive materials.[25] In air purification, induction heating may also enable rapid viral inactivation via the reported joule heating on heated filters[26] and other potential electrostatic effects on airborne pathogens, which have not been studied.

Electromagnetic wave-absorbing materials are of paramount importance for electromagnetic inducting heating. Recently,

https://doi.org/10.1021/acsami.3c18227
ACS Appl. Mater. Interfaces 2024, 16, 10148−10157

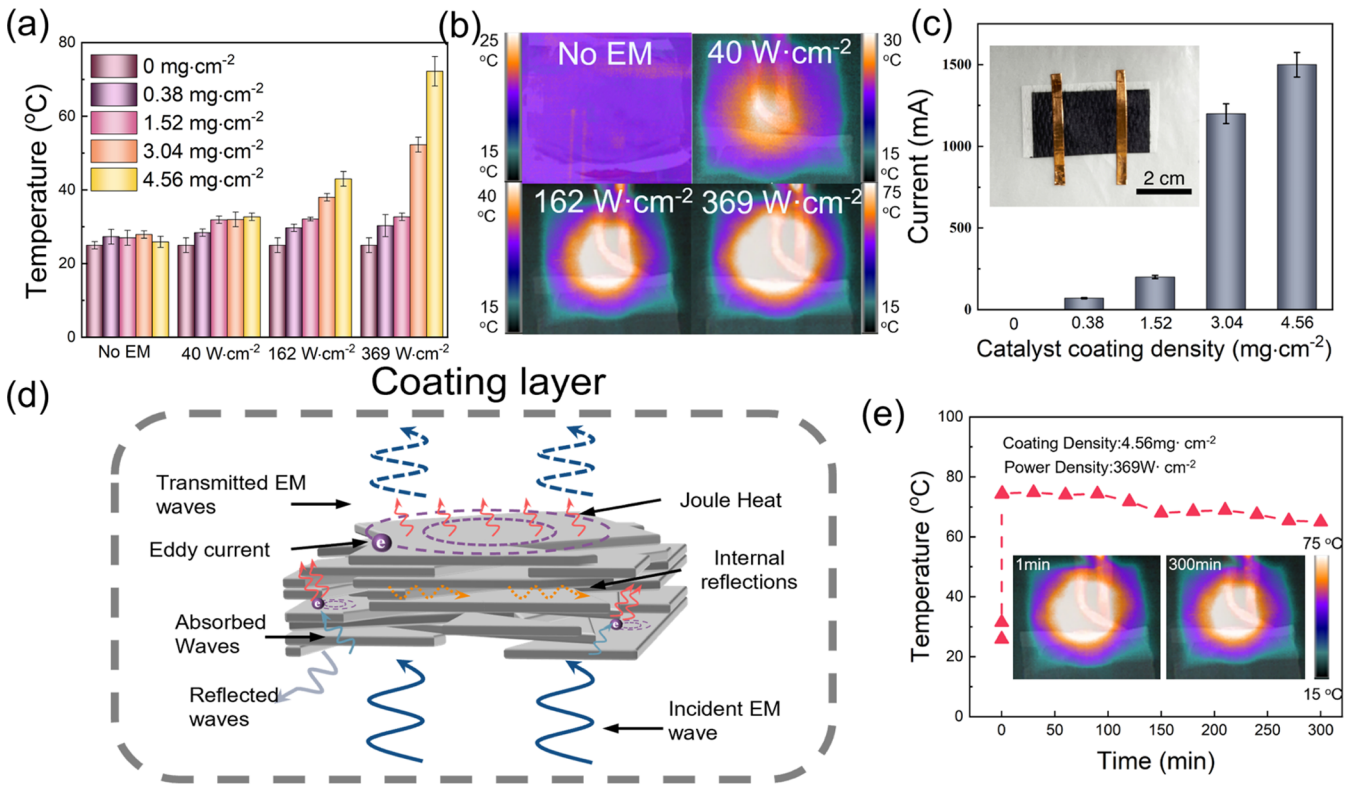

Figure 2. (a) Inductive heating of air filter with different electromagnetic power densities and MXene coating densities. (b) Thermal infrared images for MXene-coated air filters (coating density: 4.56 mg·cm^{-2}) under irradiation of varying electromagnetic power density. (c) The variation of current on MXene-coated air filters with different coating densities. (d) Schematic of MXene-coated air filter under electromagnetic field. (e) Temperature stability of air filter with coating density of 4.56 mg·cm^{-2} and electromagnetic power density of 369 W·cm^{-2}.

two-dimensional (2D) transition metal carbides and nitrides, commonly referred to as MXenes, have shown very promising electromagnetic wave-absorbing properties.[27] They also exhibit ultrahigh metallic conductivity (ca. 6000−24 000 S·cm^{-1}) and thermal conductivity.[28,29] Gogotsi et al. first evaluated the electromagnetic interference (EMI) shielding effectiveness of $Ti_3C_2T_x$ (T_x stands for surface termination elements such as oxygen, fluoride, or chloride), exhibiting absorption of over 92 dB in shielding effectiveness on a thin film (45 μm thickness).[28] Additionally, MXenes have been found to possess a thermal conductivity of up to 472 W·m^{-1}·K^{-1}, suggesting their excellent heat dissipation ability besides the strong microwave absorbance.[30] It is worth mentioning that MXene also showed antimicrobial activity against viruses (e.g., SARS-CoV-2) and thus can be utilized for antimicrobial coating face masks, personal protective equipment (PPE) kits, and face shields through photocatalytic and photothermal properties.[31,32] For example, a photocatalytic reactor containing TiO_2/MXene filler achieved 4.06 log removal for MS2 phage with 4.3 s residence time and relative humidity (RH) 30% at UV_{254} irradiation.[32] However, the mechanisms of inactivation of viral bioaerosols by MXene under electromagnetic induction remain elusive.

This study demonstrates the use of an MXene-based catalyst and electromagnetic induction to enhance air filtration and disinfection. Commercial nonwoven polypropylene air filters were coated with MXene nanosheets. The electric inductivity and electromagnetic inductive heating capabilities of MXene-coated air filters were then evaluated to elucidate the mechanisms of virus removal in a simulated bioaerosol. The study further examined the impact of MXene coating density, electromagnetic power density, and relative humidity on the viral removal efficiency and filtration stability. Furthermore, the nonthermal effects of the electromagnetic field on viral removal and inactivation were analyzed by COMSOL simulation. Overall, this innovative technology showcases significant potential in combating the persistent threat of airborne viruses and other pathogens and ensures the maintenance of safe indoor air quality.

RESULTS AND DISCUSSION

Characterization of $Ti_3C_2T_x$ MXene and MXene-Coated Filter. A high-resolution transmission electron microscopy (HRTEM) image of a single layer of as-synthesized $Ti_3C_2T_x$ MXene nanosheets is shown in Figure 1a. The enlarged HRTEM image and the selected area electron diffraction (SAED) pattern (Figure 1b and inset) indexed with a hexagonal crystal system confirm the crystallinity of synthesized $Ti_3C_2T_x$. Atomic force microscopy (AFM) images (Figure 1c) confirm that the thickness of the as-synthesized $Ti_3C_2T_x$ MXene nanosheets (red region) was 1.6 ± 0.3 nm. This thickness is slightly higher than the theoretical thickness of a $Ti_3C_2T_X$ single layer (~1 nm), probably because our MXene nanosheet did not attach to the substrate surface as a flat layer or had some folded structures or edges. Figure 1d shows the surface morphology of pristine nonwoven air filter and MXene-coated filters with different coating densities. A higher coating density (e.g., >3.04 mg·cm^{-2}) was shown to yield a more uniform MXene coating on the fiber. The cross-sectional image (Figure S4) proved the conjugation of MXene onto the filter surface. The energy-dispersive X-ray spectrom-

https://doi.org/10.1021/acsami.3c18227
ACS Appl. Mater. Interfaces 2024, 16, 10148−10157

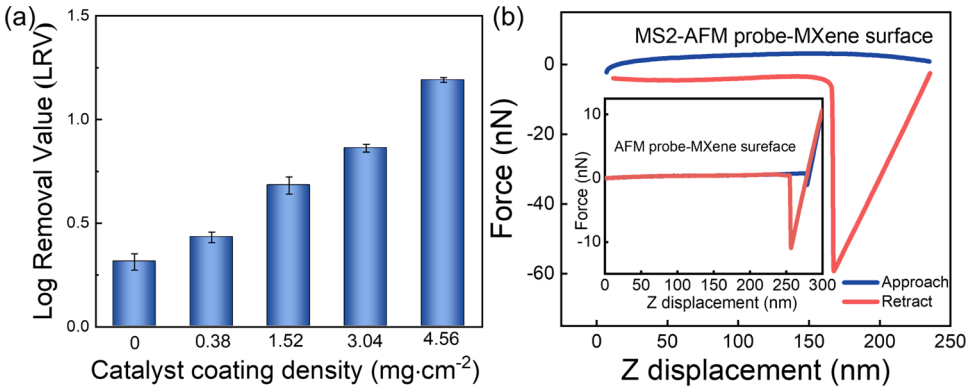

Figure 3. (a) Log removal value of MS2 phage with different MXene coating density at an air flow rate of 4 L·min^{-1}. (b) Interaction force between the MS2-modified AFM probe and the MXene surface in ambient air (temperature: 25 °C, moisture: 56%). The inset shows the interaction force curve when a pristine AFM probe was used to engage against the MXene surface.

etry (EDXS) mapping results in Figure S3 confirmed the existence of C, O, F, Cl, and Ti on the MXene-coated air filter.

Figure 1e shows the X-ray diffraction (XRD) patterns of $Ti_3C_2T_x$ MXene and polypropylene fibers with coating densities of 0, 0.38, 1.52, 3.04, and 4.56 mg·cm^{-2}. The characteristic 2θ peaks at around 7° for $Ti_3C_2T_x$ MXene (002) and at around 14.3, 17.2, 18.8, and 21.7° for polypropylene were all clearly observed.[33,34] The intensity of this (002) peak also increased as the MXene coating density increased due to the stacking of MXene sheets.[33] Similarly, the Raman spectra of uncoated and MXene-coated air filters were acquired and are compared in Figure 1f. $Ti_3C_2T_X$ had Raman signals in the range of 100 to 800 cm^{-1}.[35,36] Raman peaks near 200 cm^{-1} indicated the A_{1g} out-of-plane vibration mode of Ti and C atoms.[37] Further, the Raman signals in the range of 230−470 cm^{-1} represents in-plane (E_g) vibrations of surface groups bonded with the Ti atoms. In addition, the peaks between 600−800 cm^{-1} are related to the carbon region of MXene. These Raman peak intensities apparently increased as the coating density increased, which further confirms the presence of MXene on the filter.

Figure 1g compares the pressure drop of MXene-coated filters, showing a linear increase with the increasing air flow rate. According to Darcy's law,[38] the slope of the linear fit between the pressure drop and the air flow rate represents the air permeability of filters. As the coating density increased, the slope of the linear fit increased slightly from 14 to 17 as the air filter pores were probably blocked by MXene nanosheets. The pore size distribution (Figure S5) revealed the mean pore size did not change significantly after coating with MXene nanosheets that did not severely block the filter pores (<5 μm).

Electromagnetic Inductive Heating Performance of the MXene-Coated Air Filter. Figure 2a presents the surface temperature increase of MXene-coated air filters under different electromagnetic induction power. The MXene-coated air filter was rapidly heated to 72.2 ± 4 °C at a coating density of 4.56 mg·cm^{-2} under the induction power of 369 W·cm^{-2} within 2 s. The temperature remained unchanged, with coating densities lower than 1.52 mg·cm^{-2}. The infrared (IR) thermal mapping of the MXene-coated air filter with a coating density of 4.56 mg·cm^{-2} (Figure 2b) shows the elevated surface temperature of filters with increased electromagnetic power density. Similarly, the inset image of Figure 2b revealed that the measured current between the Cu strips on the MXene-coated air filter at a voltage of 5 V increased significantly from 200 to 1500 mA as the coating density increased from 1.52 to 4.56 mg·cm^{-2}. This matches the observed inductive heating performance of MXene as illustrated by Figure 2d, where the MXene layer could reflect or absorb the incident electromagnetic wave or allow it to be transmitted through. The absorbed electromagnetic wave interacts with the electrical and magnetic dipoles and induces an eddy current within MXene, resulting in Joule heat.[39,40] High coating densities tend to create a more uniform MXene layer on the fibers, contributing to increased thermal conductivity and heating efficiency and thereby enhancing the electromagnetic heating performance. On the other hand, increasing the coating density involves the stacking of MXene nanosheets, which in turn enhances internal reflection of electromagnetic waves. The Joule heating stability is crucial for practical applications, and thus the temperature evolution of the MXene-coated air filter during the long-term induction heating was also monitored. Figure 2e indicates that the temperature of the MXene-coated air filter reached a plateau level of 74 °C within 2 s at an electromagnetic power density of 369 W·cm^{-2} and slightly decreased to 68 °C after 5 h due to the oxidation of MXene that affects the MXene conductivity and induction power absorption.

Antiviral Performance of MXene-Coated Air Filters via Filtration without Induction Heating. Figure 3a shows the log removal of MS2 phage with different MXene coating densities at an air flow rate of 4 L·min^{-1} and a retention time or air passage time as low as 0.005 s. Pristine nonwoven filter only attained a log removal value (LRV) of 0.31 ± 0.04, whereas the reduction of MS2 phage significantly increased as the MXene coating density increased, with LRV of 1.20 ± 0.01 when the MXene coating density was 4.56 mg·cm^{-2}. MXene nanosheets enhanced the removal performance of MS2 phage due to the strong surface interactions with MS2 viruses, including van der Waals and electrostatic interaction forces between the active surface-terminating groups (O, OH, and F) and defects present on the MXene surface and the amino acids of MS2 viruses. These interaction forces facilitated the capture of viruses onto the surface of MXene and their subsequent inactivation. Unal et al. found that $Ti_3C_2T_x$ MXene exhibited viral copy numbers reduction of 99% (2 log removal) at a concentration of 0.32 μg·mL^{-1}.[41] MXenes were expected to not only effectively adsorb spike proteins but also to modify their secondary structure, such as hydrogen shaped α helix and the β pleated sheet, which hinders their interaction with the enzyme receptors of the host.[42] However, the local heating

https://doi.org/10.1021/acsami.3c18227
ACS Appl. Mater. Interfaces 2024, 16, 10148−10157

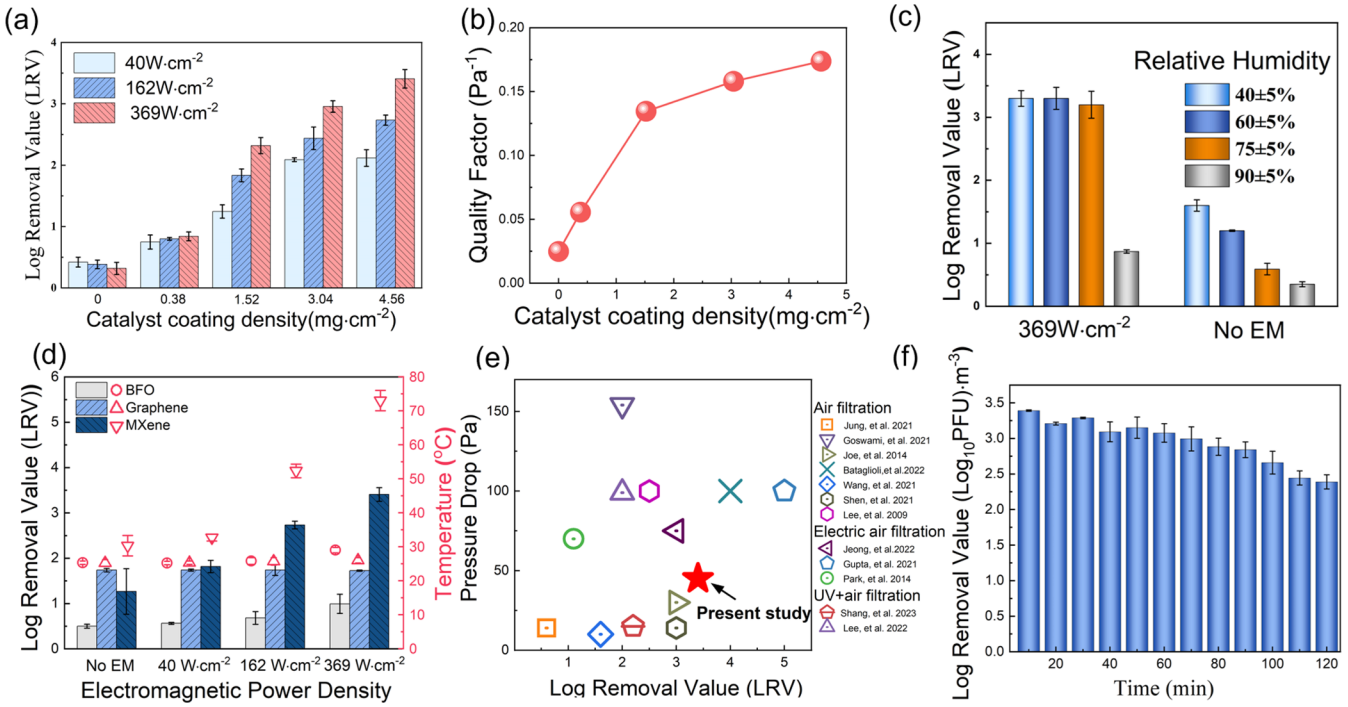

Figure 4. (a) Log removal value (LRV) of aerosol MS2 phage with different MXene coating densities and electromagnetic power densities at an air flow rate of 4 L·min^{-1} for 3 min. (b) Quality factors of MXene-coated air filter with different MXene coating densities at an electromagnetic power density of 369 W·cm^{-2}. (c) Effect of different relative humidities on filtration performance with and without electromagnetic field. (d) Viral removal performance and inductive heating of different materials under different electromagnetic power densities. (e) Antiviral performance comparison with previously reported filters. Source data are provided in Supplementary Table S2. (f) Viral removal stability of this electromagnetically enhanced air filtration system with a coating density of 4.56 mg·cm^{-2} and an electromagnetic power density of 369 W· cm^{-2}.

performance of MXenes under electromagnetic irradiation and antiviral activity were not explored previously.

To prove this concept, the interaction forces between the MXene nanosheet and MS2 viruses were examined by AFM measurements, as detailed in Section S7. Briefly, a layer of MS2 was attached onto an AFM probe that was pretreated by a cationic polymeric cross-linker, chitosan.[43] The successful conjugation of a layer of MS2 was verified by SEM images (Figure S6). Next, by advancing and retracting the AFM stylus cantilever from the MXene surface, the relative force−distance curves and gauged interaction force between the MXene surface and MS2 were captured. Figure 3b reveals that the average adhesion force (red curve) between the MXene surface and the unmodified AFM probe was found to be 12 nN (see the inset figure) in the air phases, while that between the MXene surface and the MS2-modified AFM tip became larger (60 nN). This gives direct evidence for the strong interaction of MXene and the MS2 virus. Similarly, in the water phase, the average adhesion force between the MXene surface and the MS2-modified AFM probe was larger than that of the MXene surface and unmodified AFM probes (Figure S7).

Antiviral Performance of MXene-Coated Air Filters via Filtration with Induction Heating. Figure 4a reveals that the log removal of MS2 increased with increasing MXene coating and electromagnetic power densities. The highest level of log removal of 3.4 ± 0.15 was achieved with an MXene coating density of 4.56 mg·cm^{-2} and electromagnetic power density of 369 W·cm^{-2}. However, with 0.34 mg·cm^{-2} MXene coating, the increase of electromagnetic power density did not obviously enhance the viral removal rate as the low coating density of MXene may not provide a continuous conductive pathway for the eddy currents, thereby reducing the efficiency of induction heating. In addition, high surface temperatures above 50 °C could lead to thermal destruction and inactivation of the viral components, such as surface spike proteins.[44] Jonges et al. demonstrated that the thermal inactivation of influenza viruses, specifically human influenza H3N2 and avian influenza H7N3, correlates with a diminished functionality of surface hemagglutinin and other associated glycoproteins.[45] In addition, the inductive heating accelerates aerosol evaporation and dehydration, which also contribute to viral inactivation. Liron et.al utilized COMSOL simulation to demonstrate that the evaporation time of aerosols (dimension <5 μm) is lower than 10^{-3} s.[46] Once all aerosols completely evaporate, the virions will directly be exposed to a surface temperature higher than 70 °C, which could effectively deactivate most viruses.[46,47] Interestingly, with a coating density of 1.52 mg·cm^{-2}, increasing the electromagnetic power density did not obviously change the temperature of the MXene-coated filter, but increased the LRV of MS2 phage from 1.25 to 2.32, probably due to the enhanced nonthermal effect (e.g., electromagnetic effect and electrostatic effect).

Figure S10 indicates the structural damage to MS2 viruses during the electromagnetic air filtration. The TEM image Figure S10a shows the intact round-shaped MS2 viral particles, which agrees with the typical morphology of an active MS2 virus.[48,49] After filtration, the viral concentration was substantially reduced along with some obvious morphological changes, as evidenced in Figure S10b, where irregular fragments were detected. The structural damage could result from the heating and the stress from the gas filtration. In addition, Figure 4b demonstrates that increasing the coating density enhances the quality factor from 0.02 to 0.17 Pa^{-1}, particularly at an electromagnetic power density of 369 W·

https://doi.org/10.1021/acsami.3c18227
ACS Appl. Mater. Interfaces 2024, 16, 10148−10157

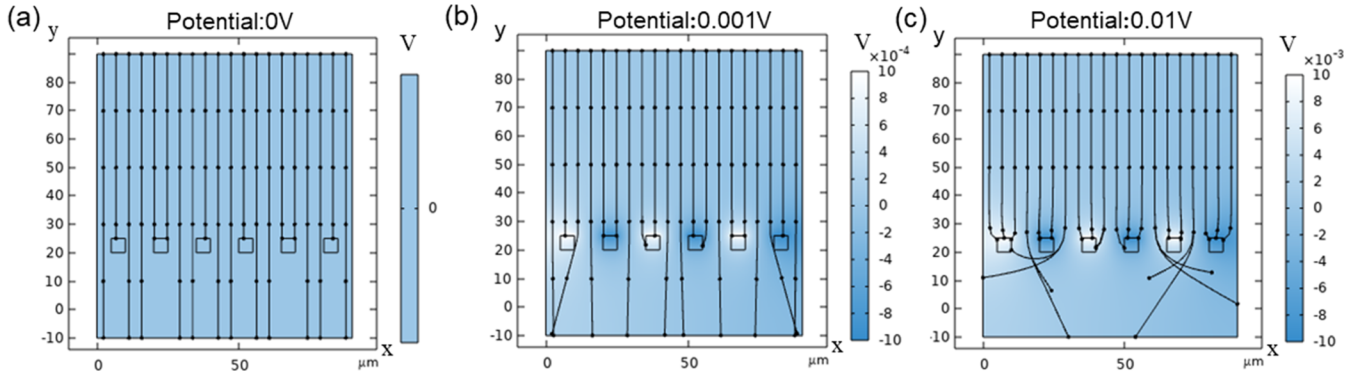

Figure 5. Trajectories of noncharged particles under electric field potential of (a) 0 V, (b) 0.001 V, and (c) 0.01 V.

cm^{-2}. This improvement leads to remarkably higher removal and offsets the minor air pressure drop increase from 29 to 45 Pa at a flow rate of 4 $L{\cdot}min^{-1}$ due to the gas flow friction rise with the MXene coating density of 4.56 $mg{\cdot}cm^{-2}$.

Humidity significantly impacts the air filtration efficiency and viral removal. This is primarily because water droplets obstruct filter pores and neutralize electrostatic effects in high-humidity environments. Figure 4c demonstrates that when the relative humidity (RH) increased from 40 ± 5 to 70 ± 5%, the change in MS2 removal was not statistically significant ($p > 0.05$) under electromagnetic induction of 369 $W{\cdot}cm^{-2}$, which may be ascribed to the evaporation of aerosols on the high-temperature filter that prevented the water clogging of filter pores. However, without electromagnetic induction, the increasing RH led to an appreciable drop of MS2 removal from 1.68 to 0.59. For both the groups with and without electromagnetic induction, a high RH of 90 ± 5% caused a significant drop in MS2 removal rates to 0.87 and 0.35, respectively. This extremely high RH may not only increase the evaporation time and heat loss[46,50] but also alter the properties of the MXene-coated filter such as electrical conductivity and thermal conductivity.

Furthermore, the viral removal performance of this MXene-coated air filter was compared to other conductive nanomaterials (graphene and $BiFeO_3$) that were similarly coated onto the same air filter at the same coating density of 4.56 $mg{\cdot}cm^{-2}$ and experimental conditions. Figure 4d shows that the $BiFeO_3$-coated filter only contributed to a slight increase of the filter temperature and LRV as the electromagnetic power density increased, probably due to its relatively weak electromagnetic adsorption at a low electromagnetic frequency (300 kHz). Nevertheless, the graphene-coated air filter achieved a relatively higher rate of MS2 removal through its sharp edges and oxidative stress,[51] while exhibiting no change in viral removal rate or inductive heating as the electromagnetic power density increased. Clearly, the MXene-coated air filter yielded the highest MS2 removal rates under the same electromagnetic induction, which yielded higher surface temperatures (e.g., over 70 °C). Figure 4e compares the antiviral performance of the electromagnetically enhanced air filter with previously reported filters. Clearly, the MXene-coated air filter yielded a high viral removal efficiency and a low air pressure drop. Notably, UV and electric air filters display a higher pressure drop (75−100 Pa) with a lower viral removal rate. In addition, filters that are coated with antiviral materials like silver and copper exhibit lower efficiency in viral removal through achieving lower pressure drop.

Finally, a short-term stability test was conducted for this MXene-coated filter to examine the potential influence of filter aging or integrity on MS2 removal. Figure 4f demonstrates that LRV slightly decreased from 3.24 to 2.39 after 120 min. The chemical composition change of MXene was analyzed by XPS before and after filtration for 120 min under an electromagnetic power density of 369 $W{\cdot}cm^{-2}$. Table S1 and Figure S8 summarize the detailed survey spectra of Ti, oxygen (O), fluorine (F), carbon (C), and chlorine (Cl). Figure S9 shows the X-ray photoelectron spectroscopy (XPS) spectra of Ti 2p and 1 s of MXene at different filtration times. The Ti 2p components at about 454.7, 456.2, 458.4, 460.6, and 462.0 eV are associated with Ti−C ($2p_{3/2}$), Ti(II) ($2p_{3/2}$), Ti−O ($2p_{3/2}$), Ti(II) ($2p_{1/2}$), and Ti−C ($2p_{1/2}$), respectively.[52,53] After induction heating filtration, the formation of TiO_2 suggested the minor oxidation of MXene in the presence of water droplets and oxygen. The O 1 s core levels are fitted by components corresponding to the O−Ti, C−Ti−Ox, and C−Ti-(OH)x bonds located at ∼529.5, 530.7, and 531.6 eV, respectively.[52,54] The peak area of C−Ti−Ox increased after induction heating filtration because the oxidation process obviously increased the number of oxygen-containing functional groups (such as − COOH and − C═O) on the surface of the MXene.

Viral Removal Mechanisms. The removal mechanisms of particulate matter via filtration may include sieving, gravity settling, inertial impaction, interception, diffusion, and electrostatic attraction. However, traditional fibrous filters, such as nonwoven polypropylene filters, suffer from the weak capture ability for bioaerosols or ultrafine submicron particles. The coating of MXene could enhance the filtration performance via the surface-terminating groups (−O, −OH, and −F) bound on the MXene nanosheet surface that renders a strong interaction with aerosol particles. In addition, MXene potentially causes irreversible viral inactivation via denaturation of the spike proteins and their secondary structure. Under the electromagnetic induction field, local surface heating further aided in viral inactivation by damaging viral proteins and nucleic acid. Second, aerosol evaporation rapidly occurs when the aerosol particles that carry viruses contact the high-temperature fibers, which also accelerates viral inactivation.

In addition to the above mechanisms, when an electromagnetic field is applied to a conductive MXene, local eddy currents may form and create a local nonuniform induced electric field. The additional electric field may alter the motion of aerosol MS2 when it passes through the MXene-coated air filter via the phenomenon of dielectrophoresis (DEP),[55] where

https://doi.org/10.1021/acsami.3c18227
ACS Appl. Mater. Interfaces 2024, 16, 10148−10157

the dielectric neutral particles such as MS2 experience charge polarization when it is immersed in the nonuniform electric field. The induced charges interact with the field to create a net force, resulting in dielectrophoretic motion. Under this motion, aerosol MS2 could be more effectively removed by impaction or interception on the filter. Dielectrophoresis has been used in the separation of proteins, exosomes, bacteria, yeast, stem cells, cancer cells, and blood cells based on the differences of their dielectric property and size.[56]

Our study employed COMSOL simulation to analyze the effect of the dielectrophoretic force on the moving trajectories of noncharged particles (i.e., MS2 viruses) as defined in Section S11. Briefly, the particles entered this field from the top boundary at a uniform flow rate of 100 $\mu m \cdot s^{-1}$. There are six squares or rectangular blocks to represent MXene-coated polypropylene fibers, which exhibit alternating positive or negative potentials under a nonuniform induced electric field. The electric potential induced on the MXene surface was approximately 0.01 V, as calculated by the electromagnetic heating module described in Section S11.1. As the induced electric potential on the polypropylene fibers increased from 0 to 0.01 V (Figure 5a–c), the moving trajectories of the noncharged particles were obviously influenced as indicated by the black line shift. In ambient aerosol samples, viral particles such as MS2 may exhibit negative charges, enhancing their susceptibility to dielectrophoretic forces. This heightened charge-based interaction significantly improves the efficiency of separation and capture methods.

As shown in eq S1, the dielectrophoretic force is proportional to toward area gradient of the squared magnitude of the nonuniform electric field ($\nabla|E|^2$), attributing to the altered motion of the particles. Figure S12a shows that the dielectrophoretic force in the x direction on the particle gradually increased up to 2.3×10^{-15} N when the particle approached the Mxene-coated filter. Equation S1 also shows that the amount of dielectrophoretic force that a particle experienced is proportional to the droplet size, our simulation result in Figure S12b verified that particles with a larger diameter are subjected to a greater dielectrophoretic force than that of a smaller particle.

CONCLUSIONS

In summary, we have developed a low-pressure-drop nonwoven air filter coated with MXenes that demonstrates impressive electromagnetically enhanced aerosol viral removal. The coating layer of $Ti_3C_2T_x$ MXene (4.56 $mg \cdot cm^{-2}$) significantly improved the inductive heating of the air filters that reached a temperature up to 72.2 ± 4 °C under an induction power density of 369 $W \cdot cm^{-2}$. A viral log removal rate of 3.4 ± 0.15 was also achieved under an aerosol flow rate of 4 $L \cdot min^{-1}$ with a spiked MS2 concentration of 10^5 $PFU \cdot mL^{-1}$. Without this induction field, the MXene-coated air filter also achieved a higher viral log removal rate (up to 1.20 ± 0.01) via surface adsorption compared to pristine air filter (0.31 ± 0.04). While MXene demonstrates commendable stability in electromagnetic inductive heating during short-term air filtration, it is important to note its vulnerability to oxidation, particularly at elevated temperatures. This susceptibility is a significant limitation for the long-term efficacy of MXene-based air filters, as highlighted by the observed decline in performance over extended use. Future studies should prioritize investigating methods to improve the stability and durability of MXene in air filtration applications. For example, a sandwich-structured MXene composite film could be achieved via the casting process by utilizing a nonwoven fabric (NWF) substrate and waterproof thermoplastic polyurethane (TPU) onto the surface of the MXene functional layer that could improve antioxidation and durability.[57] COMSOL simulations were also used to investigate the effect of dielectrophoresis on the trajectories of noncharged particles with different strengths of induced electric field. Compared with the high-frequency (2.45 GHz) microwave irradiation, this presented air filtration system using a low-frequency (300 kHz) electromagnetic irradiation offers comparable air disinfection performance with higher safety and adaptability for air disinfection in commercial buildings, hospitals, transportation systems (e.g., train station/airports), and any enclosed high-population space.

EXPERIMENTAL SECTION

Preparation and Characterization of MXene and MXene-Coated Air Filter. $Ti_3C_2T_x$ MXene was prepared by selectively etching the Al element from the corresponding Ti_3AlC_2 MAX powder (Jilin 11 Technology Co., Ltd., Jilin, China). Briefly, 10 g lithium fluoride (LiF) powder (purity ≥ 99%, Sigma–Aldrich) was added into 100 mL HCl (9 M) and stirred until completely dissolved. Afterward, 10 g of Ti_3AlC_2 MAX powder was added to the LiF/HCl mixed solution and stirred vigorously with a water bath temperature of 35 °C for 12 h. Then, the mixture was washed repeatedly with distilled water, centrifuged (3500 rpm), and decanted until the pH of the supernatant reached approximately 6. The obtained suspension was then sonicated at 40 kHz and 15 W (Branson, CPX2800H) for delamination over 30 min. Finally, the suspension was centrifuged at 3500 rpm for 30 min, and the supernatant fluid comprising a colloidal solution of delaminated $Ti_3C_2T_x$ flakes with a concentration of 8.0 $mg \cdot mL^{-1}$ was collected.

Nonwoven polypropylene filters (4 cm × 4 cm) were obtained from the middle layer of surgery masks. MXene flakes were coated on these filters through a spray coating process. Typically, the delaminated $Ti_3C_2T_x$ solution was sprayed onto the nonwoven polypropylene filters by an airbrush (Master Airbrush Model G-233) at 120 °C. Using a nozzle of 0.5 mm and an operating pressure of 80 psi, the airbrush was positioned perpendicularly to the substrate at a distance of 20 cm. The airbrush was manually moved at an approximate speed of 15 $cm \cdot s^{-1}$ in various directions to ensure uniform film deposition. The MXene loading densities were controlled as 0.38, 1.52, 3.04, and 4.56 $mg \cdot cm^{-2}$ by tuning the volume of the MXene solution used. The coated filters were vacuum-dried at 80 °C for a duration of 24 h, as shown in Figure S1. Graphene and bismuth ferrate ($BiFeO_3$) were used as electromagnetic responsive materials to coat on nonwoven filters with same coating method to compare the viral removal performances of these different induction heating catalysts. The surface morphology of MXene nanosheets coated filters with different coating densities was characterized by field emission scanning electron microscopy coupled with energy-dispersive spectroscopy (SEM-EDS, JEOL JSM-7900F).

Bacteriophage Preparation and Characterization. The freeze-dried bacteriophage MS2 powder (ATCC 15597B1) was sourced from ATCC Company. Detailed procedures for the revival and propagation of MS2 can be found in Section S2. In summary, the standard double-layer agar method was used to enumerate MS2 using Tryptic Soy Agar (BD Difco 236950, Cat.DF0369176), with the MS2 concentration being ascertained via the plaque-forming unit (PFU).[58] Plates displaying between 20 and 300 plaques were chosen for counting. All equipment and glassware employed for MS2 cultivation and propagation underwent sterilization through autoclaving. Each test was conducted three times.

The morphology of the phage particles before and after treatments was analyzed using transmission electron microscopy (TEM, JEOL JEM-F200) operating at an accelerated voltage of 200 kV. The material crystallization structure and chemical components were also

https://doi.org/10.1021/acsami.3c18227
ACS Appl. Mater. Interfaces 2024, 16, 10148–10157

analyzed by Raman spectroscopy (DXR Microscope, Thermo Scientific, Waltham, Massachusetts) and XRD (Empyrean, Malvern Panalytical, United Kingdom). Atomic force microscopy (AFM) was used to observe single-layer MXene nanosheets and measure the interaction force between the MS2 virus and the MXene-coated filters. The conductivity of the MXene-coated polypropylene air filter was evaluated by measuring the current between two Cu tapes with a distance of 2 cm at a voltage of 5 V. Typically, the MXene-coated polypropylene air filter was cut to a width of 2 cm. Two Cu tape strips with a width of 1 mm were attached to the coated air filter at a distance of 2 cm, which were then connected to the DC power supply at a voltage of 5 V via alligator clips. A multimeter connected in series with the power supply facilitated real-time current measurements.

Experimental Platform of the Electromagnetically Enhanced Air Filtration System. Figure S2 shows the photos of the benchtop air filtration system that was equipped with a 6-jet refillable collision nebulizer (CH Technologies, ARGBLM18) to produce the MS2-spiked bioaerosol with a mass median aerodynamic diameter (MMAD) of 2.5 μm. The air filtration system was made of a syringe barrel with an effective cross-sectional area of 7 cm^2 and a needle hub that were connected with a nonwoven air filter between them. Two acrylic sheets, polypropylene screws, and parafilm were used to prevent air leaks. This air filter chamber was placed above the center of an induction coil panel with an inner and outer diameter of 8 and 40 mm, respectively. An EMF generation system (ULTRAHEAT SM-5/200, UltraFlex Power Technologies, Inc.) was used to generate induction on the coil. A Biosampler (SKC INC. 225-9595) was used to collect the treated bioaerosol directly into a liquid buffer (e.g., 20 mL of PBS solution). A vacuum pump (SKC BioLite+, 228-9615) was used to maintain a constant air flow rate of 4 $L{\cdot}min^{-1}$ (pressure: −67 kPa and room temperature: 25 ± 2 °C). To investigate the pressure drop when different coated filters were inserted, an air pressure meter (Leaton) (PASCO) was installed at both ends of an air filtration system to record the inlet and outlet pressures. A humidity sensor (Weewooday, model, China) was used to monitor the relative humidity (RH) of the inlet/outlet air, which was stable at 60 ± 5%. To simulate different RH environments, sterilized cotton was introduced to dry the air flow, followed by the addition of a commercial humidifier. The resulting inlet air had two relative humidity levels of 40 ± 5% and 90 ± 5%, respectively.[59]

Evaluation of MS2 Inactivation. The MS2 suspension was added to the 6-jet refillable collision nebulizer containing 50 mL of the 1X PBS to yield an initial concentration of approximately ~10^5 $PFU{\cdot}mL^{-1}$. The performances of MS2 inactivation by this electromagnetically enhanced air filtration system were evaluated using different nonwoven filters with MXene coating densities of 0.38, 1.52, 3.04, and 4.56 $mg{\cdot}cm^{-2}$ and different electromagnetic power densities of 40, 162, and 369 $W{\cdot}cm^{-2}$. The same air flow rate of 4 $L{\cdot}min^{-1}$ was applied, and the inlet/outlet air samples were taken after a filtration time of 3 min to ensure stable air filtration and capture of the bioaerosol. All of the tests were performed in triplicate. The MS2 concentration in the aerosol was measured by using a plaque-forming unit ($PFU{\cdot}m^{-3}$). To quantify the viral concentration changes before and after the filtration, the air samples collected in the biosampler were cultivated as introduced in Section 2.2. ImageJ counted by the log removal value (LRV) of the bioaerosol MS2 phage is as follows

$$\mathrm{LRV} = \log\left(\frac{N_t}{N_0}\right) \tag{1}$$

where N_t is the MS2 concentration in the aerosol after the above-mentioned filtration conditions and N_0 is the MS2 concentration in the aerosol without going through the air filter and electromagnetic induction. The overall filtration performance of a filter can be evaluated by calculating the quality factor, QF, (Pa^{-1}) as defined below

$$\mathrm{QF} = \frac{-\ln(N_t/N_0)}{\Delta P} \tag{2}$$

where ΔP is pressure drop (Pa), which was determined by the pressure difference between the upstream and downstream of air filter.

Verification of the Chemical Stability and Antiviral Activity under Long-Term Operation. The stability of the Mxene coating (4.56 $mg{\cdot}cm^{-2}$) on the air filter was investigated through 12 consecutive filtration cycles at the air flow rate of 4 $L{\cdot}min^{-1}$ for 10 min per cycle (total 120 min) with the initial MS2 concentration of ~10^5 $PFU{\cdot}m^{-3}$. The chemical stability and antiviral activity were both investigated by X-ray photoelectron spectroscopy (XPS, Thermo K-Alpha) and the above bioassay.

COMSOL Simulation of Viral Transport Trajectories under Electromagnetic Waves. To simulate the dielectrophoretic forces acting on the neutral charged aerosol MS2 phage droplets and their location on the surface of the MXene-coated air filter, a time-dependent two-dimensional model with electrostatics module and particle tracing module were employed in COMSOL Multiphysics. The theory concept, model geometry, and material parameters are provided in Section S10.[60]

■ ASSOCIATED CONTENT

Supporting Information

The Supporting Information is available free of charge at https://pubs.acs.org/doi/10.1021/acsami.3c18227.

Preparation of MXene-coated air filter, revival and propagation of MS2, experimental platform of the air filtration system, SEM, Raman spectroscopy, AFM, XPS, TEM, and COMSOL simulation details (PDF)

■ AUTHOR INFORMATION

Corresponding Authors

Mengqiang Zhao − *Otto H. York Department of Chemical and Materials Engineering, New Jersey Institute of Technology, Newark, New Jersey 07102-1982, United States*; Email: mz24@njit.edu

Wen Zhang − *John A. Reif, Jr. Department of Civil and Environmental Engineering and Otto H. York Department of Chemical and Materials Engineering, New Jersey Institute of Technology, Newark, New Jersey 07102-1982, United States*; orcid.org/0000-0001-8413-0598; Email: wen.zhang@njit.edu

Authors

Fangzhou Liu − *John A. Reif, Jr. Department of Civil and Environmental Engineering, New Jersey Institute of Technology, Newark, New Jersey 07102-1982, United States*

Qingquan Ma − *John A. Reif, Jr. Department of Civil and Environmental Engineering, New Jersey Institute of Technology, Newark, New Jersey 07102-1982, United States*; orcid.org/0000-0001-6879-6410

Md Mohidul Alam Sabuj − *Otto H. York Department of Chemical and Materials Engineering, New Jersey Institute of Technology, Newark, New Jersey 07102-1982, United States*; orcid.org/0009-0006-2625-4772

Shih-Hsiang Yen − *Otto H. York Department of Chemical and Materials Engineering, New Jersey Institute of Technology, Newark, New Jersey 07102-1982, United States*

Dheeban Govindan − *Otto H. York Department of Chemical and Materials Engineering, New Jersey Institute of Technology, Newark, New Jersey 07102-1982, United States*

Jianan Gao − *John A. Reif, Jr. Department of Civil and Environmental Engineering, New Jersey Institute of Technology, Newark, New Jersey 07102-1982, United States*; orcid.org/0000-0003-1255-1240

https://doi.org/10.1021/acsami.3c18227
ACS Appl. Mater. Interfaces 2024, 16, 10148−10157

Menachem Elimelech − *Department of Chemical and Environmental Engineering, Yale University, New Haven, Connecticut 06520-8286, United States;* orcid.org/0000-0003-4186-1563

Complete contact information is available at: https://pubs.acs.org/10.1021/acsami.3c18227

Author Contributions

F.L.: Conceptualization, data curation, formal analysis, investigation, methodology, writing—original draft. Q.M.: Material characterization, writing. M.M.A.S.: Preparation of MXene-coated filters, writing. S.-H.Y.: XRD analysis for MXene-coated filter, writing. D.G.: Raman analysis, writing. J.G.: Writing, figure, and TOC layout. M.-Q.Z.: Writing—review and editing M.E.: Writing—review and editing W.Z.: Writing—review and editing.

Notes

The authors declare no competing financial interest.

■ ACKNOWLEDGMENTS

This study was partially supported by EPA P3 grant (SV84041901), New Jersey Health Foundation Grants (Award#: PC 27-23 and PC 55-23), NSF Molecular Separation (Award number: 2025374), NJIT Technology Innovation Translation and Acceleration (TITA) Seed Grant, and Undergraduate Research Innovation (URI) phase I and II grants at NJIT.

■ REFERENCES

(1) Liu, F.; Ma, Q.; Marjub, M. M.; Suthammanont, A. K.; Sun, S.; Yao, H.; Tao, Y.; Zhang, W. Reactive Air Disinfection Technologies: Principles and Applications in Bioaerosol Removal. *ACS ES&T Eng.* **2023**, *3*, 602−615, DOI: 10.1021/acsestengg.3c00016.

(2) Lednicky, J. A.; Lauzardo, M.; Fan, Z. H.; Jutla, A.; Tilly, T. B.; Gangwar, M.; Usmani, M.; Shankar, S. N.; Mohamed, K.; Eiguren-Fernandez, A.; et al. Viable SARS-CoV-2 in the air of a hospital room with COVID-19 patients. *Int. J. Infect. Dis.* **2020**, *100*, 476−482.

(3) Brady-Estévez, A. S.; Kang, S.; Elimelech, M. A single-walled-carbon-nanotube filter for removal of viral and bacterial pathogens. *Small* **2008**, *4* (4), 481−484.

(4) Park, D.-U.; Yeom, J.-K.; Lee, W. J.; Lee, K.-M. Assessment of the levels of airborne bacteria, gram-negative bacteria, and fungi in hospital lobbies. *Int. J. Environ. Res. Public Health* **2013**, *10* (2), 541−555.

(5) Kim, S.; Chung, J.; Lee, S. H.; Yoon, J. H.; Kweon, D.-H.; Chung, W.-J. Tannic acid-functionalized HEPA filter materials for influenza virus capture. *Sci. Rep.* **2021**, *11* (1), No. 979.

(6) Jung, S.; Yang, J.-Y.; Byeon, E.-Y.; Kim, D.-G.; Lee, D.-G.; Ryoo, S.; Lee, S.; Shin, C.-W.; Jang, H. W.; Kim, H. J.; Lee, S. Copper-coated polypropylene filter face mask with SARS-COV-2 antiviral ability. *Polymers* **2021**, *13* (9), 1367.

(7) Joe, Y. H.; Woo, K.; Hwang, J. Fabrication of an anti-viral air filter with SiO2−Ag nanoparticles and performance evaluation in a continuous airflow condition. *J. Hazard. Mater.* **2014**, *280*, 356−363.

(8) Joe, Y. H.; Yoon, K. Y.; Hwang, J. Methodology for modeling the microbial contamination of air filters. *PLoS One* **2014**, *9* (2), No. e88514.

(9) Barnewall, R. E.; Bischoff, W. E. Removal of SARS-CoV-2 bioaerosols using ultraviolet air filtration. *Infect. Control Hosp. Epidemiol.* **2021**, *42* (8), 1014−1015.

(10) Gupta, A.; Sharma, C. P.; Thamaraiselvan, C.; Pisharody, L.; Powell, C. D.; Arnusch, C. J. Low-Voltage Bacterial and Viral Killing Using Laser-Induced Graphene-Coated Non-woven Air Filters. *ACS Appl. Mater. Interfaces* **2021**, *13* (49), 59373−59380.

(11) Park, M.; Son, A.; Chua, B. Microorganism-ionizing respirator with reduced breathing resistance suitable for removing airborne bacteria. *Sens. Actuators, B* **2018**, *276*, 437−446.

(12) Huo, Z.-Y.; Kim, Y.-J.; Suh, I.-Y.; Lee, D.-M.; Lee, J. H.; Du, Y.; Wang, S.; Yoon, H.-J.; Kim, S.-W. Triboelectrification induced self-powered microbial disinfection using nanowire-enhanced localized electric field. *Nat. Commun.* **2021**, *12* (1), No. 3693.

(13) Woo, M.-H.; Grippin, A.; Wu, C.-Y.; Wander, J. Microwave-irradiation-assisted HVAC filtration for inactivation of viral aerosols. *Aerosol Air Qual. Res.* **2012**, *12* (3), 295−303.

(14) McDevitt, J. J.; Milton, D. K.; Rudnick, S. N.; First, M. W. Inactivation of Poxviruses by Upper-Room UVC Light in a Simulated Hospital Room Environment. *PLoS One* **2008**, *3* (9), No. e3186.

(15) McDevitt, J. J.; Rudnick, S. N.; Radonovich, L. J. Aerosol Susceptibility of Influenza Virus to UV-C Light. *Appl. Environ. Microbiol.* **2012**, *78* (6), 1666.

(16) Kumar N, S.; Grekov, D.; Pré, P.; Alappat, B. J. Microwave mode of heating in the preparation of porous carbon materials for adsorption and energy storage applications−an overview. *Renewable Sustainable Energy Rev.* **2020**, *124*, No. 109743.

(17) Hou, T.; Wang, B.; Jia, Z.; Wu, H.; Lan, D.; Huang, Z.; Feng, A.; Ma, M.; Wu, G. A review of metal oxide-related microwave absorbing materials from the dimension and morphology perspective. *J. Mater. Sci.: Mater. Electron.* **2019**, *30*, 10961−10984.

(18) Wei, R.; Wang, P.; Zhang, G.; Wang, N.; Zheng, T. Microwave-responsive catalysts for wastewater treatment: A review. *Chem. Eng. J.* **2020**, *382*, No. 122781.

(19) Wang, X.; Liu, F.; Liang, W.; Zhang, W. Characterization of electromagnetic catalysis and degradation of algogenic odor using Fe3O4 nanoparticles with tannin coating. *ACS ES&T Eng.* **2021**, *1* (11), 1542−1552.

(20) Liu, F.; Ma, Q.; Marjub, M. M.; Suthammanont, A. K.; Sun, S.; Yao, H.; Tao, Y.; Zhang, W. Reactive Air Disinfection Technologies: Principles and Applications in Bioaerosol Removal. *ACS ES&T Eng.* **2023**, *3* (5), 602−615.

(21) Timko, B. P.; Whitehead, K.; Gao, W.; Kohane, D. S.; Farokhzad, O.; Anderson, D.; Langer, R. Advances in drug delivery. *Annu. Rev. Mater. Res.* **2011**, *41*, 1−20.

(22) Hedayatnasab, Z.; Abnisa, F.; Daud, W. M. A. W. Review on magnetic nanoparticles for magnetic nanofluid hyperthermia application. *Mater. Des.* **2017**, *123*, 174−196.

(23) Qing, W.; Hu, Z.; Ma, Q.; Zhang, W. Conductive Fe3O4/PANI@ PTFE membrane for high thermal efficiency in interfacial induction heating membrane distillation. *Nano Energy* **2021**, *89*, No. 106339.

(24) Wang, W.; Tuci, G.; Duong-Viet, C.; Liu, Y.; Rossin, A.; Luconi, L.; Nhut, J.-M.; Nguyen-Dinh, L.; Pham-Huu, C.; Giambastiani, G. Induction heating: An enabling technology for the heat management in catalytic processes. *ACS Catal.* **2019**, *9* (9), 7921−7935.

(25) Bayerl, T.; Duhovic, M.; Mitschang, P.; Bhattacharyya, D. The heating of polymer composites by electromagnetic induction−A review. *Composites, Part A* **2014**, *57*, 27−40.

(26) Stanford, M. G.; Li, J. T.; Chen, Y.; McHugh, E. A.; Liopo, A.; Xiao, H.; Tour, J. M. Self-sterilizing laser-induced graphene bacterial air filter. *ACS Nano* **2019**, *13* (10), 11912−11920.

(27) Cao, M.-s.; Cai, Y.-Z.; He, P.; Shu, J.-C.; Cao, W.-Q.; Yuan, J. 2D MXenes: electromagnetic property for microwave absorption and electromagnetic interference shielding. *Chem. Eng. J.* **2019**, *359*, 1265−1302.

(28) Shahzad, F.; Alhabeb, M.; Hatter, C. B.; Anasori, B.; Man Hong, S.; Koo, C. M.; Gogotsi, Y. Electromagnetic interference shielding with 2D transition metal carbides (MXenes). *Science* **2016**, *353* (6304), 1137−1140.

(29) Zhou, B.; Zhang, Z.; Li, Y.; Han, G.; Feng, Y.; Wang, B.; Zhang, D.; Ma, J.; Liu, C. Flexible, robust, and multifunctional electromagnetic interference shielding film with alternating cellulose nanofiber and MXene layers. *ACS Appl. Mater. Interfaces* **2020**, *12* (4), 4895−4905.

(30) Zha, X.-H.; Zhou, J.; Zhou, Y.; Huang, Q.; He, J.; Francisco, J. S.; Luo, K.; Du, S. Promising electron mobility and high thermal conductivity in Sc 2 CT 2 (T = F, OH) MXenes. *Nanoscale* **2016**, *8* (11), 6110−6117.
(31) Huang, Z.; Cui, X.; Li, S.; Wei, J.; Li, P.; Wang, Y.; Lee, C.-S. Two-dimensional MXene-based materials for photothermal therapy. *Nanophotonics* **2020**, *9* (8), 2233−2249.
(32) Liu, L.; laghari, A. A.; Meng, G.; Meng, G.; Chen, H.; Chen, H.; Wang, C.; Wang, C.; Xue, Y. Photocatalytic disinfection of different airborne microorganisms by TiO2/MXene filler: Inactivation efficiency, energy consumption and self-repair phenomenon. *J. Environ. Chem. Eng.* **2022**, *10* (3), No. 107641.
(33) Shao, H.; Lin, Z.; Xu, K.; Taberna, P.-L.; Simon, P. Electrochemical study of pseudocapacitive behavior of Ti3C2Tx MXene material in aqueous electrolytes. *Energy Storage Mater.* **2019**, *18*, 456−461.
(34) Ariyoshi, S.; Hashimoto, S.; Ohnishi, S.; Negishi, S.; Mikami, H.; Hayashi, K.; Tanaka, S.; Hiroshiba, N. Broadband terahertz spectroscopy of cellulose nanofiber-reinforced polypropylenes. *Mater. Sci. Eng. B* **2021**, *265*, No. 115000.
(35) Huang, H.; Su, H.; Zhang, H.; Xu, L.; Chu, X.; Hu, C.; Liu, H.; Chen, N.; Liu, F.; Deng, W.; et al. Extraordinary areal and volumetric performance of flexible solid-state micro-supercapacitors based on highly conductive freestanding Ti3C2Tx Films. *Adv. Electronic Mater.* **2018**, *4* (8), No. 1800179.
(36) Guo, R.; Yuan, P.; Han, X.; He, X.; Lu, J.; Li, Q.; Dang, L.; Sun, J.; Liu, Z.; Lei, Z. Thickness-Independent Capacitive Performance of Holey Ti3C2Tx Film Prepared through a Mild Oxidation Strategy. *Small* **2023**, *19* (9), No. 2205947.
(37) Sarycheva, A.; Gogotsi, Y. Raman spectroscopy analysis of the structure and surface chemistry of Ti3C2T x MXene. *Chem. Mater.* **2020**, *32* (8), 3480−3488.
(38) Liu, C.; Dai, Z.; He, B.; Ke, Q.-F. The effect of temperature and humidity on the filtration performance of electret melt-blown nonwovens. *Materials* **2020**, *13* (21), 4774.
(39) Liu, T.; Zhang, N.; Zhang, K.; Wang, Y.; Qi, Y.; Zong, M. Multi-components matching manipulation of MXene/PPy@ β2-SiW11Co/Fe3O4 nanocomposites for enhancing electromagnetic wave absorption performance. *Composites, Part A* **2022**, *159*, No. 107020.
(40) Pan, F.; Yu, L.; Xiang, Z.; Liu, Z.; Deng, B.; Cui, E.; Shi, Z.; Li, X.; Lu, W. Improved synergistic effect for achieving ultrathin microwave absorber of 1D Co nanochains/2D carbide MXene nanocomposite. *Carbon* **2021**, *172*, 506−515.
(41) Unal, M. A.; Bayrakdar, F.; Fusco, L.; Besbinar, O.; Shuck, C. E.; Yalcin, S.; Erken, M. T.; Ozkul, A.; Gurcan, C.; Panatli, O.; et al. 2D MXenes with antiviral and immunomodulatory properties: A pilot study against SARS-CoV-2. *Nano Today* **2021**, *38*, No. 101136.
(42) Ghasemy, E.; Miri Jahromi, A.; Khedri, M.; Zandi, P.; Maleki, R.; Tayebi, L. In-silico study on viability of MXenes in suppressing the coronavirus infection and distribution. *J. Biomol. Struct. Dyn.* **2022**, *40* (21), 11460−11466.
(43) Deacon, M. P.; McGURK, S.; Roberts, C. J.; WILLIAMS, P. M.; TENDLER, S. J.; DAVIES, M. C.; Davis, S.; HARDING, S. E. Atomic force microscopy of gastric mucin and chitosan mucoadhesive systems. *Biochem. J.* **2000**, *348* (3), 557−563.
(44) Bertrand, I.; Schijven, J.; Sánchez, G.; Wyn-Jones, P.; Ottoson, J.; Morin, T.; Muscillo, M.; Verani, M.; Nasser, A.; de Roda Husman, A.; et al. The impact of temperature on the inactivation of enteric viruses in food and water: a review. *J. Appl. Microbiol.* **2012**, *112* (6), 1059−1074.
(45) Jonges, M.; Liu, W. M.; van der Vries, E.; Jacobi, R.; Pronk, I.; Boog, C.; Koopmans, M.; Meijer, A.; Soethout, E. Influenza virus inactivation for studies of antigenicity and phenotypic neuraminidase inhibitor resistance profiling. *J. Clin. Microbiol.* **2010**, *48* (3), 928−940.
(46) Issman, L.; Graves, B.; Terrones, J.; Hosmillo, M.; Qiao, R.; Glerum, M.; Yeshurun, S.; Pick, M.; Goodfellow, I.; Elliott, J.; Boies, A. Filtration of viral aerosols via a hybrid carbon nanotube active filter. *Carbon* **2021**, *183*, 232−242.
(47) Chin, A. W. H.; Chu, J. T.; Perera, M. R.; Hui, K. P.; Yen, H.-L.; Chan, M. C.; Peiris, M.; Poon, L. L. Stability of SARS-CoV-2 in different environmental conditions. *Lancet Microbe* **2020**, *1* (1), No. e10.
(48) Kim, K.; Narayanan, J.; Sen, A.; Chellam, S. Virus Removal and Inactivation Mechanisms during Iron Electrocoagulation: Capsid and Genome Damages and Electro-Fenton Reactions. *Environ. Sci. Technol.* **2021**, *55* (19), 13198−13208.
(49) Yang, C.; Wen, L.; Li, Y.; Li, X.-y. Fabrication of SnO2-Sb reactive membrane electrodes for high-efficiency electrochemical inactivation of bacteria and viruses in water. *Chem. Eng. J.* **2022**, *446*, No. 137327.
(50) Liu, F.; Li, Y.; Hao, S.; Cheng, Y.; Zhan, Y.; Zhang, C.; Meng, Y.; Xie, Q.; Xia, H. Well-aligned MXene/chitosan films with humidity response for high-performance electromagnetic interference shielding. *Carbohydr. Polym.* **2020**, *243*, No. 116467.
(51) Goswami, M.; Yadav, A. K.; Chauhan, V.; Singh, N.; Kumar, S.; Das, A.; Yadav, V.; Mandal, A.; Tiwari, J. K.; Siddiqui, H.; et al. Facile development of graphene-based air filters mounted on a 3D printed mask for COVID-19. *J. Sci.: Adv. Mater. Devices* **2021**, *6* (3), 407−414.
(52) Han, M.; Yin, X.; Wu, H.; Hou, Z.; Song, C.; Li, X.; Zhang, L.; Cheng, L. Ti3C2MXenes with modified surface for high-performance electromagnetic absorption and shielding in the X-band. *ACS Appl. Mater. Interfaces* **2016**, *8* (32), 21011−21019.
(53) Halim, J.; Lukatskaya, M. R.; Cook, K. M.; Lu, J.; Smith, C. R.; Näslund, L.-Å.; May, S. J.; Hultman, L.; Gogotsi, Y.; Eklund, P.; Barsoum, M. W. Transparent conductive two-dimensional titanium carbide epitaxial thin films. *Chem. Mater.* **2014**, *26* (7), 2374−2381.
(54) Wang, X.; Shen, X.; Gao, Y.; Wang, Z.; Yu, R.; Chen, L. Atomic-scale recognition of surface structure and intercalation mechanism of Ti3C2X. *J. Am. Chem. Soc.* **2015**, *137* (7), 2715−2721.
(55) Farid, A.; Najafi, A.; Browning, J.; Smith, E. B. Electromagnetic waves' effect on airflow during air sparging. *J. Contam. Hydrol.* **2019**, *220*, 49−58.
(56) Sarno, B.; Heineck, D.; Heller, M. J.; Ibsen, S. D. Dielectrophoresis: Developments and applications from 2010 to 2020. *Electrophoresis* **2021**, *42* (5), 539−564.
(57) Liu, J.-J.; Yang, W.-J.; Xu, Y.; Yuen, A. C. Y.; Chen, T. B. Y.; Wei, C.-X.; Zhu, S.-E.; Yeoh, G.-H.; Yang, W.; Lu, H.-D. MXene-based films via scalable fabrication with improved mechanical and antioxidant properties for electromagnetic interference shielding. *Compos. Commun.* **2022**, *31*, No. 101112.
(58) Wu, X.; Tang, A.; Bi, X.; Nguyen, T. H.; Yuan, B. Influence of algal organic matter of Microcystis aeruginosa on ferrate decay and MS2 bacteriophage inactivation. *Chemosphere* **2019**, *236*, No. 124727.
(59) Jeong, S. B.; Lee, D. U.; Lee, B. J.; Heo, K. J.; Kim, D. W.; Hwang, G. B.; MacRobert, A. J.; Shin, J. H.; Ko, H. S.; Park, S. K.; et al. Photobiocidal-triboelectric nanolayer coating of photosensitizer/silica-alumina for reusable and visible-light-driven antibacterial/antiviral air filters. *Chem. Eng. J.* **2022**, *440*, No. 135830.
(60) Borgelink, B.; Carchia, A.; Hernández-Sánchez, J.; Caputo, D.; Gardeniers, J.; Susarrey-Arce, A. Filtering efficiency model that includes the statistical randomness of non-woven fiber layers in facemasks. *Sep. Purif. Technol.* **2022**, *282*, No. 120049.

https://doi.org/10.1021/acsami.3c18227
ACS Appl. Mater. Interfaces 2024, 16, 10148−10157